A NOVEL RATIOMETRIC METHOD FOR DETERMINING THE CONSEQUENCES OF CELL-SIZED FEATURES IN A MICROFLUIDIC GENERATOR OF CONCENTRATION GRADIENTS

By

Arunan Skandarajah

Thesis

Submitted to the Faculty of the

Graduate School of Vanderbilt University

in partial fulfillment of the requirements

for the degree of

MASTER OF SCIENCE

in

Biomedical Engineering

December, 2009

Nashville, Tennessee

Approved:

Professor John P. Wikswo

Professor Chris J. Janetopoulos

ACKNOWLEDGEMENTS

I have to begin with the professors and advisors who made this research possible. I would like to thank Professor John Wikswo for offering me the first hints of science's true complexity and for the practical components of securing funding, providing resources, and serving as a reader of this work. I greatly appreciated the direction and focus Professor Christopher Janetopoulos provided, the time he set aside to discuss all manner of scientific issues, and his input in my writing process. I will always be indebted to Phil Samson for being willing to transfer to me some of his considerable expertise, for his patience, and for assistance throughout my project. I would like to offer my gratitude to Professor Robert Roselli for his assistance with this work and throughout my graduate career at Vanderbilt. I would like to thank Professor Shane Hutson for several thoughtful discussions, as well.

Over the course of my research, the guidance that Dr. Carrie Elzie and Ron Reiserer provided has been invaluable, as have Dr. Kevin Seale's questions on the nature of a scientist. I appreciate Adit Dhummakupt's help with the facilities, especially at odd times of the day. I would like to thank Holley Lynch and Sarah Earl for assistance with confocal microscopy and Professor Dmitry Koktysh at the Vanderbilt Institute of Nanoscale Science and Engineering for spectrophotometry training. Other members of the Vanderbilt Institute for Integrative Biosystems Research and Education (VIIBRE), including Don Berry and Allison Price, have been incredible technical and editorial resources.

I cannot thank my friends enough for sticking with me through all the times I could not be back by a reasonable hour. Last, but certainly not least, I would like to thank my family for providing the strength, day-to-day encouragement, and inspiration that drove me to finish this project.

LIST OF TABLES

LIST OF FIGURES

TABLE OF CONTENTS

CHAPTER I

INTRODUCTION

With the advent of rapid prototyping, microfluidic systems have come to represent a new paradigm for the study of biology with single-cell resolution and incredibly high throughput [1-3]. These systems have gained prominence in the field for several reasons: reduced reagent consumption; precision of device manufacture; automation and rapid control of experimental conditions; and compactness of the systems themselves. Many of the most recent and inexpensive generations of microfluidic devices utilize soft lithography of poly(dimethylsiloxane), or PDMS, a well-characterized, optically transparent, biologically inert polymer well suited for the patterning of complex geometries. Much of the physics and practical considerations of transitioning to culturing and assaying cells on this scale has been elucidated in recent years [3-5]. With this knowledge and any one of a number of devices that provide tunable chemical stimuli, researchers can probe the pathways of cell signaling that underlie complex behaviors including morphogenesis, the immune response, and wound healing [6-8]. These systems have also been generalized and characterized in detail, allowing for robust spatiotemporal control of signaling molecule concentration [9, 10].

Beyond control of the single parameter of concentration, microfabricated structures can also be constructed to constrain cells in three dimensions through fairly simple one- or two-layer fabrication, better mimicking the complexity of the cells' native environments [11]. This is important because as cells detect chemical cues, they also integrate mechanical signals into their responses. Systems incorporating both stimuli can then help explain the variety of cellular

behaviors that have multiple inputs. For example, integrated responses have been shown to govern stem cell fate and differential proliferation in tissue constructs [11, 12]. Even in studies that focus on response to gradients of concentration, there is a growing emphasis on replicating the cellular microenvironment to make results more representative and *in vivo*-like [13].

Geometric features that control the cellular microenvironment, however, must be fabricated on the scale of the cells they influence. While producing these features is not at the limit of current fabrication techniques, the features themselves can confound the results provided by the increasingly complex assays that study cell motility in response to chemical signaling. Current methods for numerical gradient analysis and optical gradient quantification make certain assumptions that must be re-examined in the face of using sophisticated microfabricated tools. In this work, we consider three particular factors using a modern chemotaxis system. First, we demonstrate that the introduction of microstructures alters both chemical and mechanical cues, making it difficult to tease apart what combination of the two triggers the cellular response. Second, we evaluate a multi-dye method for ratiometric correction specific to individual fields of view. This is presented as an improvement over standard flat-field correction in addressing field-specific height variation and edge effects [14]. Finally, we expand upon excellent prior work that considered the effects of cell geometry on gradient formation at this scale [15]. While this earlier work analyzed artifacts introduced by a single cell under different flow regimes, we demonstrate the variation in gradient formation as a function of cell loading density and cell height in a diffusion dominated system. This work aims to provide tools and analysis to aid in the design of systems that manipulate and probe the cellular microenvironment.

CHAPTER II

A NOVEL RATIOMETRIC METHOD FOR DETERMINING THE CONSEQUENCES OF CELL-SIZED FEATURES IN A MICROFLUIDIC GENERATOR OF CONCENTRATION GRADIENTS

Arunan Skandarajah[1,2]
Christopher J. Janetopoulos[2,3,4]
John P. Wikswo[1,2,5,6]
Philip C. Samson[2,5]

[1]Department of Biomedical Engineering
Vanderbilt University
Nashville, TN

[2]Vanderbilt Institute for Integrative Biosystems Research and Education
Vanderbilt University
Nashville, TN

[3]Department of Biological Sciences
Vanderbilt University
Nashville, TN

[4]Department of Cell and Developmental Biology
Vanderbilt University
Nashville, TN

[5]Department of Physics and Astronomy
Vanderbilt University
Nashville, TN

[6]Department of Molecular Physiology and Biophysics
Vanderbilt University
Nashville, TN

Corresponding Author:
Philip Samson
Physics and Astronomy
Box 1807, Station B
Vanderbilt University
Nashville, TN 37235

615-343-4124
FAX: 615-322-4977
philip.samson@vanderbilt.edu

Introduction

The ability of cells to detect and migrate directionally in response to a gradient in chemical stimuli is known as chemotaxis. This phenomenon underlies physiologically relevant behaviors in humans such as morphogenesis, wound healing, the immune response, and metastasis [7, 8, 16, 17]. In addition to its role in mammalian systems, chemotactic processes are pervasive in other organisms, as well. Experiments conducted on model systems such as the social amoeba *Dictyostelium discoideum* have helped elucidate the conserved mechanisms which regulate chemotaxis [18, 19]. Established devices used to study chemotaxis, including the Boyden, Zigmond, and Dunn chambers [20-22], continue to provide insight into cellular behavior in these and other contexts. As researchers have sought a more comprehensive and quantitative understanding of the chemotactic response, the tools to assay chemotaxis have themselves become more varied and precise. A major advance predicated on microfluidic technology was the active-flow gradient generator from Jeon et al., which was fabricated by standard soft lithography and offered the ability to create complex gradients and either maintain or rapidly switch them as necessary [6, 7, 23]. Systems based on the active mixing of a gradient for application to cells have become widespread and have been characterized analytically by several groups including our own [9, 10, 24]. While these recent works demonstrate the precision with which gradients can be produced, modeled, and used to explain observed behavior, cells are actually integrating far more than just an individual chemical signal to drive their motility. The most recently designed chemotaxis assay chips have sought to address two particular confounding factors: flow-induced shear stress and cell-substrate interactions.

Flow, whether applied by microfluidic systems or *in vivo*, has been demonstrated to alter

the migration of cells during their response to chemotactic stimuli. For example, experimental and numerical analysis of the micromixer introduced by Jeon et al. demonstrated that increasing shear stress reduced expected chemotaxis while introducing a migration component in the downstream direction [25]. For the *in vivo* case of wound healing, the laminar stress in blood vessels has been shown to enhance endothelial cell motility to the wound site [16]. More recent microfluidic systems have corrected for this complicating factor by either reducing convection in the region of the cells with high-resistance impediments or by eliminating flow entirely by returning to a passively driven system with gradients produced by diffusion in the absence of convection. Examples of high-resistance impediments include a hydrogel layer that effectively shields an existing gradient from the pressure associated with loading [26] and the use of multiple layer heights to make transport by diffusion dominant over that by convection [27]. Devices that are sealed during observation to eliminate flow, such as the one analyzed in this work, can maintain pseudo-steady-state gradients during a pre-determined experimental period but cannot dynamically vary the applied gradient [28].

Cell/substrate interactions are being actively elucidated by biologists seeking to understand migration within the full complexity of the body [29] and by tissue engineers using three-dimensional cues to guide cells in their devices [30]. The simplest chemotaxis assays present cells with a physiologically unrealistic substrate that is uniform and two-dimensional [21, 22]. While still working in two-dimensional space, other assays have micropatterned single layers that can control cell adhesion to explore cell to extra-cellular matrix effects on directional migration [31]. To better mimic the full three-dimensionality of cellular environments, several current systems are utilized to study migration in porous hydrogels [13, 32]. Further systems have integrated these biological gels with three-dimensional structures such as “micropegs” to

demonstrate micromechanical interactions and the resulting relationships with cellular phenotype and differentiation [12, 30].

Rapid progress in the design, modeling, and validation of these microfluidic systems offers improved tools for the study of chemotaxis. In transitioning to tools on the microfluidic scale, many differences with macroscale culturing and experimental environments have been considered, such as the relative volume of cells to media, the induced shear stress, and the high local concentrations of secreted molecules [4]. The physics of microfluidics within biological microelectromechanical systems has also been considered in great detail [3], from the dominance of diffusion over convection at these scales to pumping systems based on surface energy [33]. In the context of newer chemotaxis assays, cell-size features predominate and the cells themselves can occupy a significant portion of the volume. While the perturbation of flow by a single cell and the resulting changes in gradient formation have been studied in convection-controlled systems [15], the consequences of microstructure geometry on more complex diffusion-dominated systems have yet to be systematically elucidated.

In this work, we address the question of how gradient formation is altered by both the presence of complex microstructures and the cells themselves. We use a combination of novel imaging and modeling processes to explore this question. We first apply standard epi-fluorescence imaging and numerical modeling tools to characterize a new flow-free microfluidic device that provides both three-dimensional mechanical cues and chemical stimuli. After considering the limitations of these techniques, we utilize a novel ratiometric variation on epi-fluorescence. Unlike current single-dye ratiometric intracellular calcium measurement methods [34], we present a more flexible multi-dye solution. We then evaluate this multi-dye method in conjunction with confocal microscopy, determining whether this gives us the ability to more

accurately quantify gradient development in the region of three-dimensional structures than does traditional optical sectioning. We also detail the capability to stringently analyze edge effects that other imaging systems in less complex environments can neglect [35]. These tools may allow researchers to separate optical artifacts from the potential partitioning of the small molecules that are often used in chemotaxis assays. We also discuss the vulnerabilities of this technique and outline further experiments and variations on this ratiometric paradigm for integration with other imaging modalities. Finally, we utilize our verified computational model to consider the sensitivity of gradient formation in this device to cell loading density and aspect ratio. The approach and techniques we utilize reveal valuable information about the limitations of our particular system. This process will also be of use in the rational design of any device that guides or probes cells with a chemical gradient when the features of the device are themselves on the order of the size of the cells.

Materials and Methods

Device Design and Fabrication

The passive gradient generator (**Figure 1**) was designed in AutoCAD (Autodesk, San Rafael, CA) and fabricated through standard soft lithography procedures [1, 36]. In brief, an image was printed to a custom chrome mask (Advance Reproductions, North Andover, MA). The pattern was transferred to a silicon wafer substrate (Nova Electronic Materials, Carrollton, TX) through the process of photolithography. Negative photoresist SU8-2010 (Microchem Corp., Newton, MA) was spun to a height of 13 μm, exposed through the pattern by UV light, and developed to remove unexposed photopolymer.

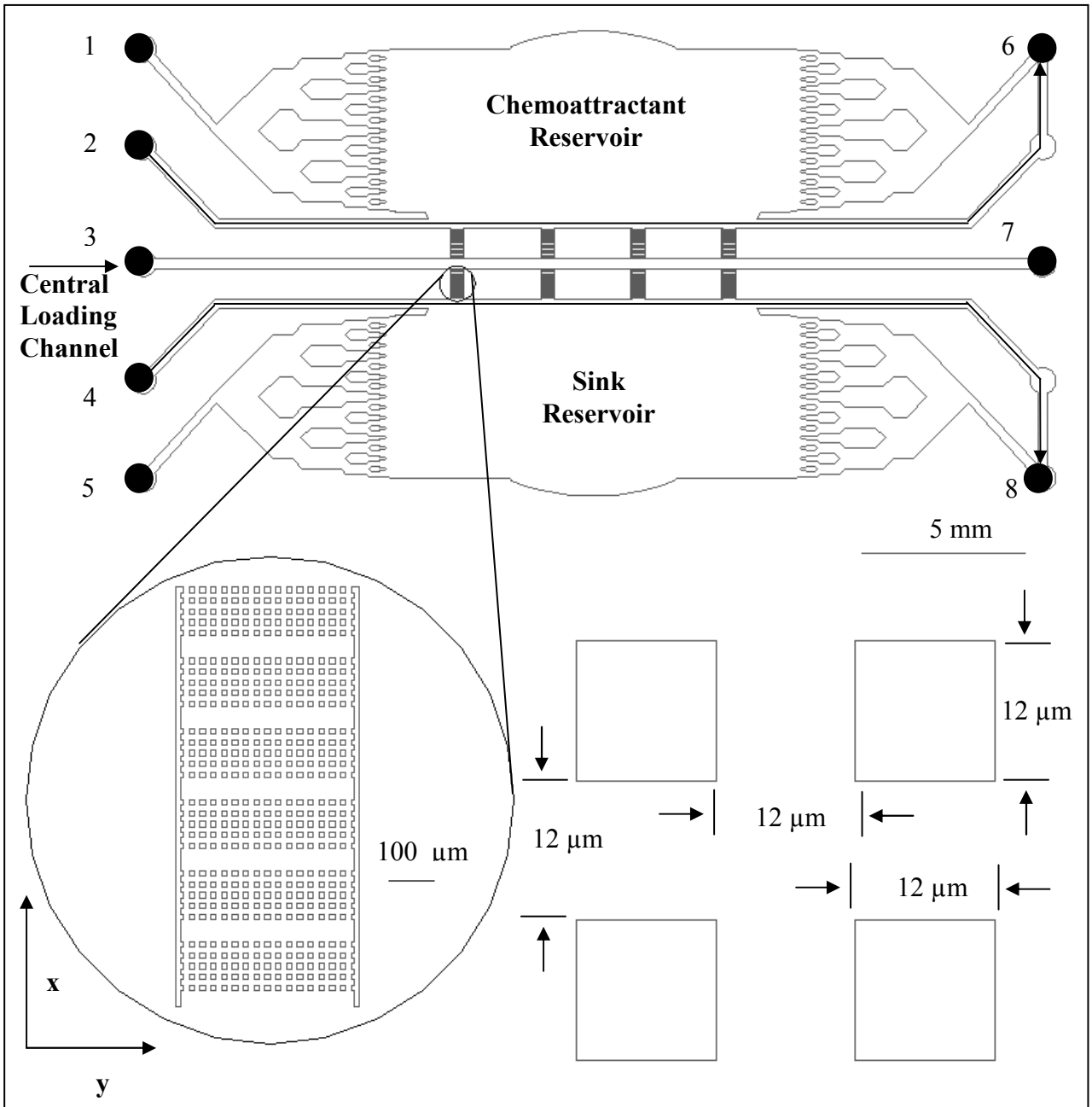

Figure 1: Schematic of the microfluidic chemotaxis device analyzed. A) An AutoCAD illustration of the entire device with the reservoirs for maximum and zero concentration indicated and sheath flow layers labeled with arrows; 25 µm circular posts used for support in the reservoir regions are omitted from the drawing for clarity. B) A close-up of the "ladder" of posts and clear regions along which the gradient forms. C) Posts and gaps are each 12 µm in the x and y dimensions.

The process was repeated to overlay an additional 20 μm of SU8 to make the two sheath flow layers connecting ports 2-6 and 4-8 **(Figure 1A**). A profilometer (Tencor Instruments Alpha-Step 200 Profilometer, Milpitas, CA) confirmed the height of the SU8 mold within a tolerance of less than 3 μm. To prevent adhesion of the cast poly(dimethylsiloxane) (PDMS) device to the mold, the photoresist structure was silanized by chemical vapor deposition of trimethylchlorosilane for at least 3 hours. PDMS (Sylgard 184, Dow Corning, Midland, MI) was prepared in a 10:1 ratio of prepolymer to curing agent, poured onto the patterned master, degassed for 20 minutes, and baked at 65 °C for at least 4 hours. Devices were separated from the silicon substrate by cutting through the PDMS on the edges of the device with a scalpel blade. Access ports 1-8 in **Figure 1A** were punched with 15 gauge stainless steel. The increased height of channels connecting ports 2 to 6 and 4 to 8 allowed for precise loading into the chemoattractant reservoir as described below. The initial cast was sectioned into thin slices and visualized to check for definition of microstructures.

To limit rapid evaporation-induced convection in the device while allowing for high magnification imaging, it was necessary to maintain near 100% humidity on a coverglass surface. To accomplish this, we utilized “chambered” coverglass which consists of a coverslip base with four plastic walls and a lid (Lab-Tek, Rochester, NY). To prepare devices for use, the PDMS device and the coverglass chamber were exposed to oxygen plasma (Harrick Plasma Cleaner/Sterilizer-32G, Pleasantville, NY) and the device was irreversibly bonded to the inner coverglass surface of the chamber. The first stage of device loading was completed at this time to maintain the hydrophilicity of the oxidized channels. After the second stage of device loading, evaporation was controlled by wetting the inside of the chamber and sealing all gaps with silicone grease before observation.

Device Loading

Alexa Fluors 488 and 568 conjugated to 10 kDa Dextran were purchased from Molecular Probes (Eugene, OR). In the first stage of device loading, an aqueous solution of 50 μM of the reference fluorophore was pipetted onto each port and was drawn into the channels by the initial hydrophilicity of the channels. The device was then maintained in a humidity controlled system for at least 4 hours to allow complete filling of the device by excess fluorophore solution on the ports.

In the second stage of device loading, the chemoattractant reservoir (**Figure 1A**) was loaded with 50 μM of the reference fluorophore as well as 50 μM of the second, diffusing fluorophore. The rest of the device was not altered at this stage, remaining loaded with only 50 μM of the reference fluorophore. Hence the reference fluorophore was maintained at a concentration of 50 μM throughout the device while the diffusing fluorophore was loaded only in the chemoattractant reservoir, from which it was allowed to diffuse. The loading process relied on surface energy driven flow [28]. Briefly, access ports 3, 4, 5, 7 and 8 in **Figure 1A** were conformally sealed with PDMS patches to prevent evaporation. A 2 μL drop containing both the reference dye and the diffusing fluorophore was placed on port 1. A solution containing only the reference dye was pipetted to a volume of 5 μL on port 2 and 12 μL on port 6. To continue the loading process, droplet volumes at ports 1 and 2 were maintained, consuming up to 15 μL of each reagent. Visualization of loading was done on a Zeiss Axiovert 25 (Carl Zeiss MicroImaging, Thornwood, NY) with a QImaging Cooled RTV Camera (Surrey, BC, Canada). After confirming the complete filling of the reservoir, the remaining ports were sealed with PDMS patches, and the device was set aside in a 100% relative humidity environment to allow diffusive gradient formation with minimal evaporation-induced convection.

Numerical Simulation of Chemical Gradient Formation

The multi-physics modeling software COMSOL (COMSOL Inc., Burlington, MA) was used to analyze the time evolution of a model molecule's distribution throughout the device. Simple Fickian diffusion governed the changing of chemical gradients over time. The initial concentration in the source reservoir was set to 100%, while the sink reservoir, cell loading channel, and migration bridges initially contained none of the molecule of interest. To reduce computational complexity and provide a clearer presentation of our findings, a representative subset of the device (**Figure 2a**) is modeled and discussed in this work. The time course of the gradient formation is dependent on the diffusion coefficient, which is specific to the chemoattractant. To make our calculations generally applicable to molecules with a known diffusion coefficient, we define a characteristic time, τ [37]

$$\tau = L^2/D \,, \qquad (1)$$

where L is the relevant length dimension and D is the diffusion coefficient of the molecule of interest. In this case, the relevant length was chosen as the distance from one reservoir to the other, approximately 2.2 mm. The simulation was conducted through a time of 6τ, corresponding to ~72 hours for the fluorophores used to validate the model. This time frame is at the limit of chemotaxis assays conducted in the device.

Before utilizing our model to analyze gradient formation, we evaluated whether we were introducing computational artifacts into our analysis by using a finite element mesh that was too coarse or by utilizing time steps that were too long. Since we expect this model to approach reality with the use of increasing spatial and temporal resolution, we evaluated our choice of finite element mesh and time step by assessing how sensitive the results of the model were to changes in meshing and time step conditions and considering the model appropriate if the results

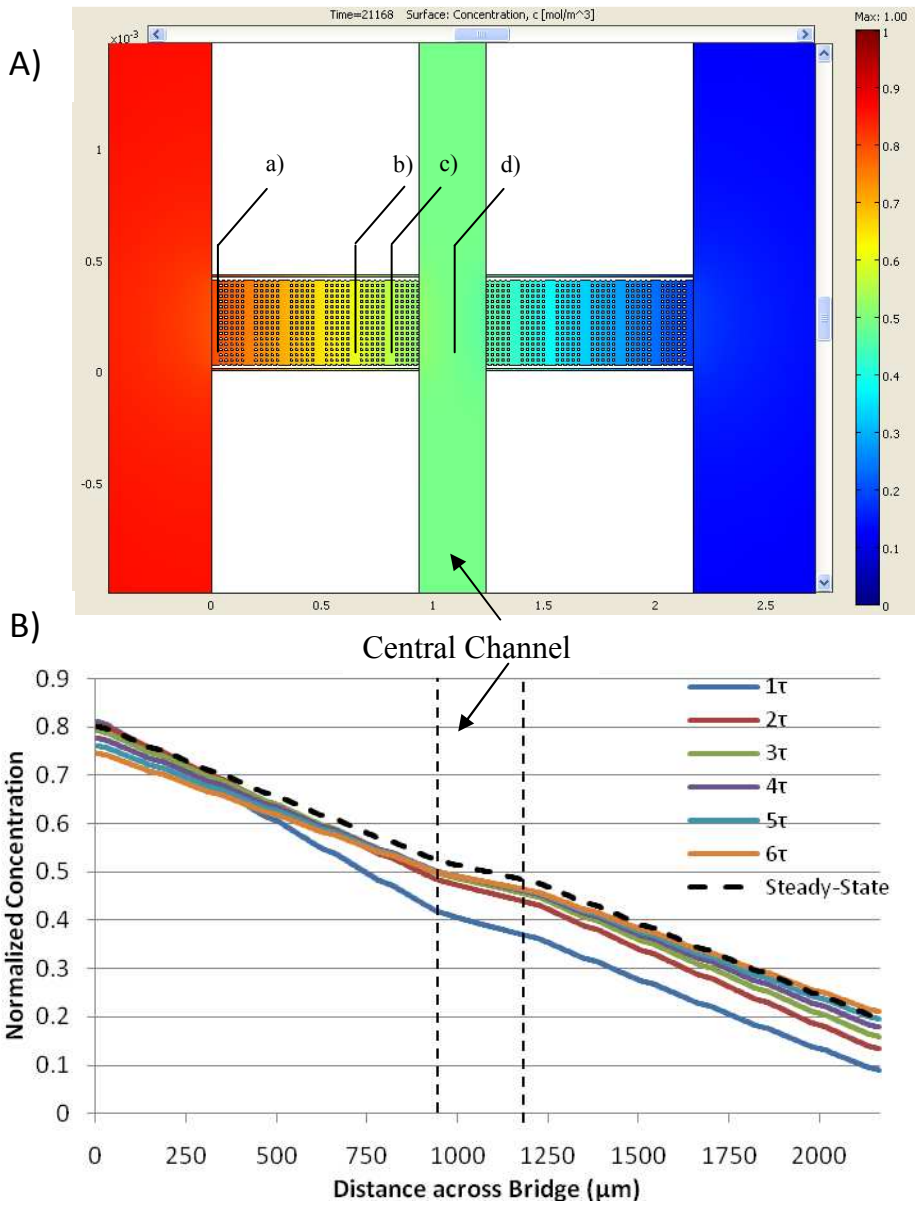

Figure 2: A) Example of the result of a finite element model conducted in COMSOL. The rows in Table 1 correspond to the error between the coarse and fine variants of the finite element model at the corresponding points a, b, c, and d. B) The time evolution of the gradient along the ladder as well as the steady-state solution for infinitely wide reservoirs.

were insensitive.

After completing this initial evaluation of the modeling process, we utilized COMSOL to evaluate the effects of PDMS microstructures, cellular occlusion, and cell density on gradient formation. Utilizing steady-state and time-dependent 2-D models, we demonstrate the relative significance of the spatial variation of the gradient caused by PDMS posts against the temporal variation over the 6τ period of interest. We then considered a pseudo-3-D model in which we approximate cell occlusion by reducing the effective diffusion constant in proportion to the volumetric occlusion. Since occlusion is a function of both cell height and channel height, this provides useful insight into the variation in the gradients that cells encounter as a function of channel aspect ratio. Finally, we used images of cells in the device to create a probabilistic cell-loading algorithm. By varying the density of cells, we demonstrate the sensitivity of both the mean and variance of the gradients in the device to cell density.

Visualization of Chemical Gradient Formation

The time evolution of the chemical gradient in the *xy* plane of the device was imaged in epi-fluorescence mode. Standard protocols were followed for maximizing dynamic range while minimizing photobleaching of the specimens [14]. Images were collected using an Axiovert 200M (Carl Zeiss MicroImaging, Thornwood, NY) equipped with a CoolSnap camera (Roper Scientific GmbH, Germany) and mercury arc lamp. The Alexa Fluor 488 was imaged using the standard FITC filter set and the Alexa Fluor 568 was imaged with a TRITC filter set.

To evaluate how the gradients depended upon the location of the imaged region within the height of the channel, we collected images at different heights on a Zeiss LSM410 laser-scanning confocal microscope. For this system, the Alexa Fluor 488 was excited by the 488 line

of an Ar/Kr laser and fluorescence was collected through a 515-540 band-pass filter. The Alexa Fluor 568 was excited by the 568 line and fluorescence was collected through a 580 long-pass filter. Images in both wide-field and confocal mode were collected using objectives optimized for flatness of field and minimal color dispersion. Images were exported as 16-bit TIFF files for further analysis.

Spectrophotometry

A Carry 5000 spectrophotometer (Varian, Palo Alto, CA) was utilized to collect the absorbance spectra across the visual spectrum for each dye utilized. A standard 1 cm path length was used to confirm the absorption spectra provided by Molecular Probes and to evaluate the degree of potential interaction among multiple fluorophores.

Two-Dimensional Standard and Ratiometric Image Processing

Images were imported into MATLAB and corrected by the standard one-color flat-field correction and by the proposed two-color ratiometric method as described below. The standard flat-field process, detailed by Murphy, involves the capture of three images: the raw frame, dark frame, and flat-field frame [14]. The raw frame consists of the unprocessed specimen image while capture of the dark frame simply follows the same protocol without the use of any excitation source. This allows for measurement of the offset signal in the CCD and provides an indication of the thermal noise. The flat-field frame is an image of a featureless and uniformly dyed region that is further smoothed by averaging several images. The flat-field frame provides information on the variation in the sensitivity of CCD pixels and uneven illumination resulting from the optics. The corrected image is obtained by carrying out the following calculation on a

pixel-by-pixel basis,

$$corrected(x,y) = M\frac{(Raw(x,y) - Dark(x,y))}{(Flat(x,y - Dark(x,y))}\ , \qquad (2)$$

where the mean value of the raw image, M, is utilized as a common scaling factor for all pixels. We describe this process as a single-color, field-flattening correction.

As an alternative to this process, we propose a multi-dye ratiometric correction that utilizes a background and a spatially dependent illumination correction specific to each field of view. The goal of this process is to correct for aberrations in illumination introduced by the particular structures in the field of view – either light-piping due to edges of PDMS features, or differences in channel heights. This process of image correction requires at least two fluorophores. The reference dye, present at a uniform concentration throughout the device, serves as an internal control for differences in the light path, channel depth, and the collection of out-of-plane fluorescence observed at the boundaries of structures and walls in microfluidic systems [35, 38]. Raw frames are captured for each fluorophore using the appropriate excitation sources and filter sets. The exposure time for each fluorophore was chosen to maximize the dynamic range and to reduce noise in the image while minimizing photobleaching. It is essential that corresponding raw frames for the multiple fluorophores be collected in the same field of view and at the same focal plane. To correct for improper registration in x-y of different channels, ImageJ (NIH, Bethesda, MD) was used to align images. Instead of subtracting a standard dark-field frame, we find the minimum pixel value in the frame and conduct a uniform subtraction. This step attempts to eliminate the baseline autofluorescence and light-piping that we expect in a field of view containing PDMS surrounded by a lower refractive index solution. If an appropriate offset is not used for each field of view, the calculated intensity would no longer be linearly related to fluorophore concentration when taking a ratio of the two frames. Finally,

we carry out a variant on the flat-field correction on a pixel-by-pixel basis,

$$corrected(x,y) = M\frac{(Raw_{Gradient}(x,y) - Background_{Gradient}(x,y))}{(Raw_{Reference}(x,y) - Background_{Reference}(x,y))} \quad . \qquad (3)$$

For both correction methods, the corresponding concentration gradients were quantified by averaging the pixels with the same *x* coordinate across the regions of the channel that lie outside the posts. For each method, this generated a single intensity value for each *x* coordinate of interest.

Three-Dimensional Ratiometric Image Processing

We demonstrate an analogous ratiometric approach to quantify gradients in the *z* dimension, *i.e.,* at different heights in the channel. Images for both fluorophores are collected using confocal microscopy, as described above. For this method to correct the images along the optical axis, we require illumination to vary in the same manner for both of these dyes as a function of height. If this condition holds, we can extract images for the corresponding focal planes for each color, and apply Equation (3) in a plane-by-plane manner in ImageJ. We evaluate this proposed method by analyzing an axial concentration profile that is theoretically uniform and consider what factors lead to the response we observe.

Results

Model Sensitivity to Meshing and Time Step Conditions

We varied the temporal and spatial resolution of the model by a factor of two in either direction from the chosen conditions and observed that the system was fairly robust against these changes. In **Table 1** we present how the calculated concentration of the diffusing molecule is

affected by extending the time steps and using a finite element mesh that was a factor of two coarser. Each area listed along the left of **Table 1** corresponds to a labeled location in **Figure 2**, and moving from top to bottom in the table corresponds to moving farther from the chemoattractant reservoir. The error at any point is fairly minimal, and while there does seem to be a higher apparent error as we move farther from the chemoattract reservoir, this results in part from presenting the percentage error instead of the absolute value. Since the chemoattractant reservoir is initially at 100% concentration while the remainder of the system is initially at 0%, the expected concentration decreases from the reservoir outward. As a practical consequence, an equal absolute error would represent a larger percentage error at increasing distances from the reservoir. Overall, there are only minor differences between the concentration values derived from the chosen conditions and those from a relaxed model, implying that there are no significant computational artifacts resulting from discretization in time or space.

Table 1 – Percent Difference Resulting from Relaxing Mesh and Time Step Conditions	$=100\%\ X\ \frac{\lvert fineModel(x,t) - coarseModel(x,t)\rvert}{fineModel(x,t)}$				
	Time Point in Simulation				
Position in Figure 2	τ/2	τ	2τ	4 τ	6 τ
a) Chemoattractant Reservoir	0.21	0.15	0.14	0.13	0.16
b) Region 1	1.37	0.48	0.43	0.02	0.05
c) Region 2	1.87	0.61	0.53	0.04	0.02
d) Central Channel	3.02	0.18	0.72	0.04	0.00

Modeling of Gradient Stability and Homogeneity

Though we develop an analysis of a pseudo-3-D device for chemotaxis, it is appropriate to simplify the model to two dimensions because of the aspect ratios of our device. The relevant maximum dimensions across which diffusion occurs are approximately 450 μm and 2.2 mm in the *xy* plane of the cells and less than 15 μm in the *z* direction. Since the time constant for diffusion in Equation (1) varies as L^2, the time scale of diffusion and equilibration in *z* is 1/1000

of that in the other two dimensions. This means that, regardless of the molecule, any variation across the height of the device would disappear almost instantly relative to the time it takes for a gradient to form between the two reservoirs.

Since the chemoattractant reservoir depletes over time, we first used our model to confirm that a sufficient gradient exists over the course of a proposed experiment. We approximated the behavior of an average protein by utilizing in our COMSOL model the known characteristics of 10 kDa dextran conjugated to a fluorophore. To generalize the results across other fluorophores, data are described in normalized time and distance across the bridge (**Figure 2**). To determine whether the time variation in the gradient would be a significant contributor to cell behavior, we also modeled the spatial variation resulting from device geometry (**Figure 3**). By focusing on a 200 μm length of the bridge spanning regions with and without posts, it becomes clear in **Figure 3A** that the concentration profile is not linear and is instead a function of local device geometry. This difference can be more readily quantified by plotting the gradient itself (**Figure 3B**) and comparing our design against an equivalent bridge with no posts. Over the time frame of interest, these two figures demonstrate that the gradient encountered by a theoretical cell is more strongly a function of spatial variation than of time.

The variation in the gradient along the length of a bridge can be replicated by replacing complex regions obstructed by posts with simple regions with diffusivity values proportional to the area that is unobstructed. This approximation can be made because spatial mass transfer is the product of flux and the cross-sectional area; a change in one will have the same effect on the product as a proportionally large change in the other. In concrete terms, a region that has 40% of

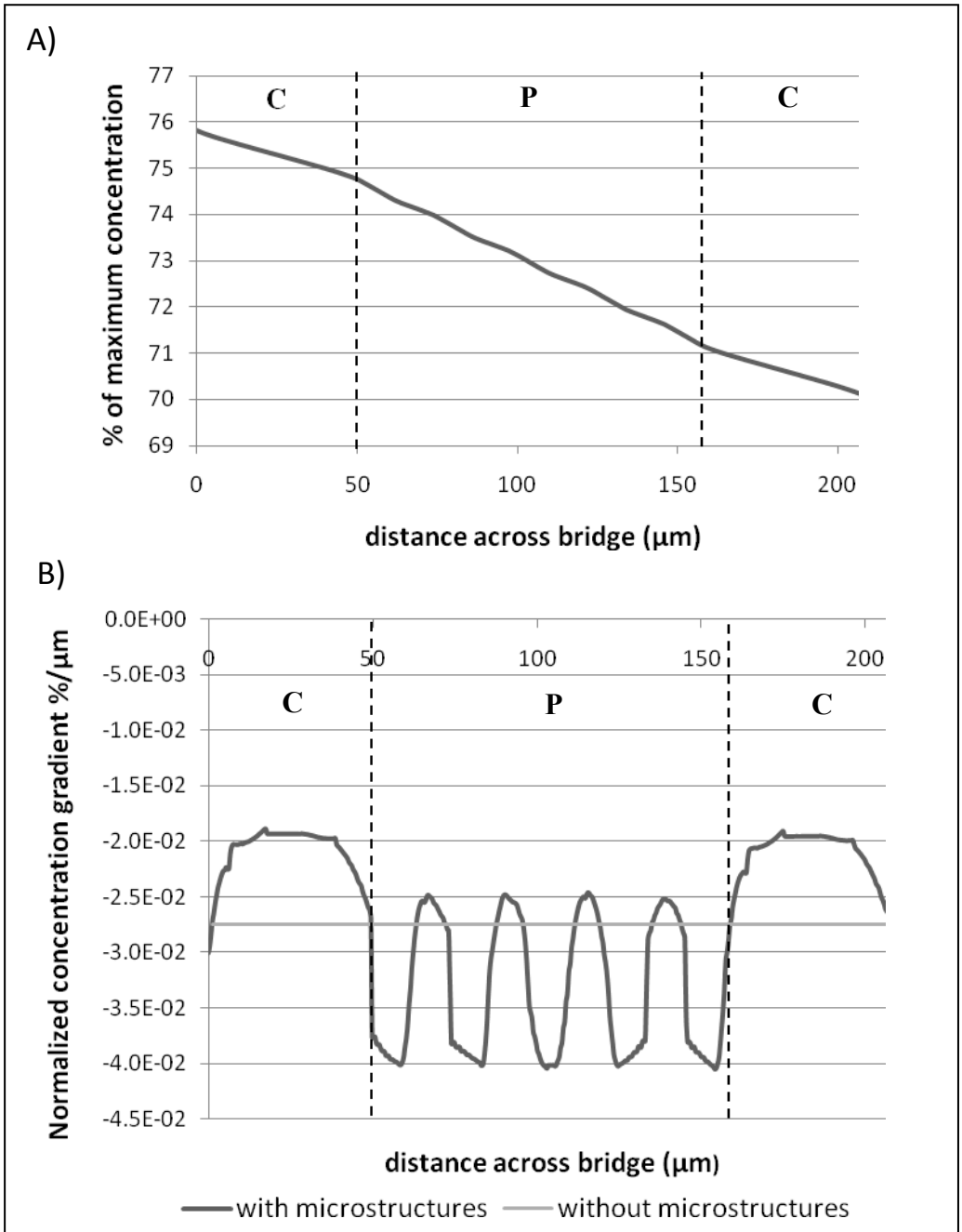

Figure 3: Concentration data from two clear regions (**C**) and one set of posts (**P**) extracted from the steady-state COMSOL model in Fig. 2. Boundaries between regions indicated with a dashed line and the maximum concentration set to the initial concentration of the chemoattractant reservoir. A) A plot of concentration versus distance across bridge demonstrates spatial variation. B) The slope of the gradient in this system is plotted in comparison to an equivalent system without post structures. The repeating higher magnitude values indicate steeper gradients in the regions between the posts as compared to the regions clear of posts.

its area occluded by posts would result in the same gradient as a region without occlusion and a diffusivity value of 60% of the unobstructed region. We extend this logic, which was described for obstruction in the *xy* plane by the posts, in a later section to model cell occlusion in the *z* dimension.

Spectrophotometry

We measured the extinction coefficients for our Alexa Fluor-tagged dextran molecules at the neutral pH used for experimentation and obtained maximum values of 104,000 and 107,000 $cm^{-1} M^{-1}$ for Alexa Fluor 488 and 568, respectively. These values are well within the order of observed values for the similar fluorophore fluorescein [39]. For maximum heights of 33 μm and maximum concentrations of 50 μM, less than 2% of the light is absorbed through the height of the sample for either fluorophore. The complete normalized absorption spectra for the two fluorophores are plotted in **Figure 4**. Within the quantitative limits of our measurement methods, these results confirm that height and concentration effects are negligible for the chosen dimensions and dilutions.

Correction of Fluorescence across Regions of Varying Channel Height

Images of a field of view containing multiple channel heights were collected and corrected as described above using both the traditional single-color flat-field correction and the multi-color ratiometric correction. While the underlying concentration gradient in the raw (**Figure 5A**) and flat-field corrected (**Figure 5B**) images is somewhat visible by eye, the most severe confounding factor is that recorded intensity also appears to be a function of channel height. The inadequacy of standard correction methods in this respect can be noted qualitatively

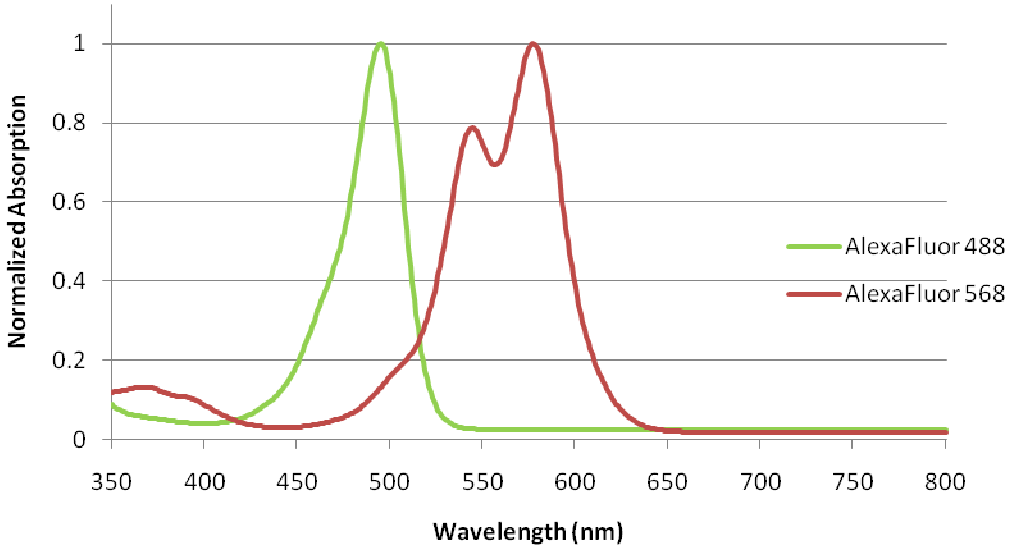

Figure 4 – Absorption spectra for the dextran conjugated AlexaFluors utilized in fluorescence experiments normalized to the maximum absorbance value for each.

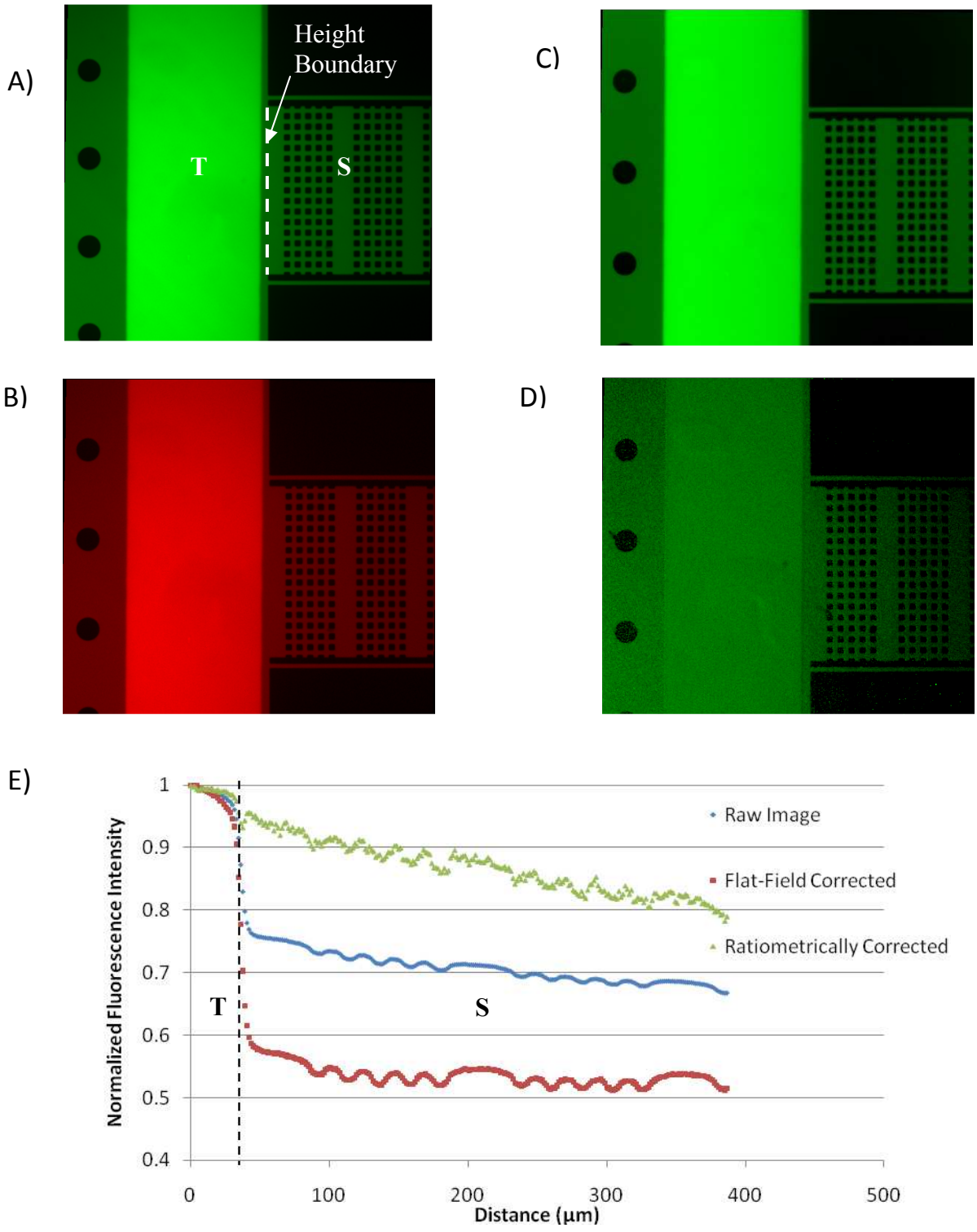

Figure 5 – Flat-field and ratiometric image correction of a field of view containing a 33 µm tall channel (**T**), corresponding to the connection between ports 4 and 8, and the 13 µm short layer (**S**). A) An uncorrected image of the gradient forming fluorophore with the height change of interest labeled. B) Image corrected by standard flat-field methods described in Eq. (2). C) An uncorrected image of the reference fluorophore. D) Image corrected by the two-color ratiometric method described in Eq. (3). E) Normalized intensity profiles generated along the direction of the gradient beginning at the boundary between the two layers, indicated with a dotted line, and continuing to right-hand edge of the image.

by tracing the intensity across a height boundary in **Figure 5A,** where we see that there is a significant decrease in fluorescence intensity that cannot be explained by simple diffusion. This could result from collection of the more significant out-of-plane fluorescence in the taller regions. With the use of an image of the reference fluorophore (**Figure 5C**), maintained at constant concentration throughout the device, we derive a ratiometrically corrected image in **Figure 5D.**

In **Figure 5E** we quantify the results of the two methods of image correction with respect to differences in channel height by plotting the normalized average pixel intensity along the length of the bridge. The raw image demonstrates a significant decrease in intensity at the boundary, as expected from a qualitative assessment of **Figure 5A**. The flat-field correction seems to worsen the intensity difference at the boundary. In practical terms, this means that the original field of view was illuminated such that there was a gradient in illumination intensity that opposed the direction of the expected gradient; correcting for this error increases the apparent difference between the short and tall regions of the channel, but this accentuation is an artifact of the direction of the illumination gradient and not inherent to the flat-field correction itself. In contrast, quantification of the ratiometrically corrected image, **Figure 5D**, yields a more linear intensity profile without an abrupt change at the height boundary.

Correction of Fluorescence Intensity in the Proximity of PDMS Microstructures

Even in fields of view with constant height, we find that aberrations introduced by field-specific illumination and edge effects near the microstructures are significant. As in **Figure 5**, the four images in **Figure 6A-D** correspond to the raw, flat-field corrected, reference, and ratiometrically corrected versions of a single field of view, respectively. **Figure 6E** was created

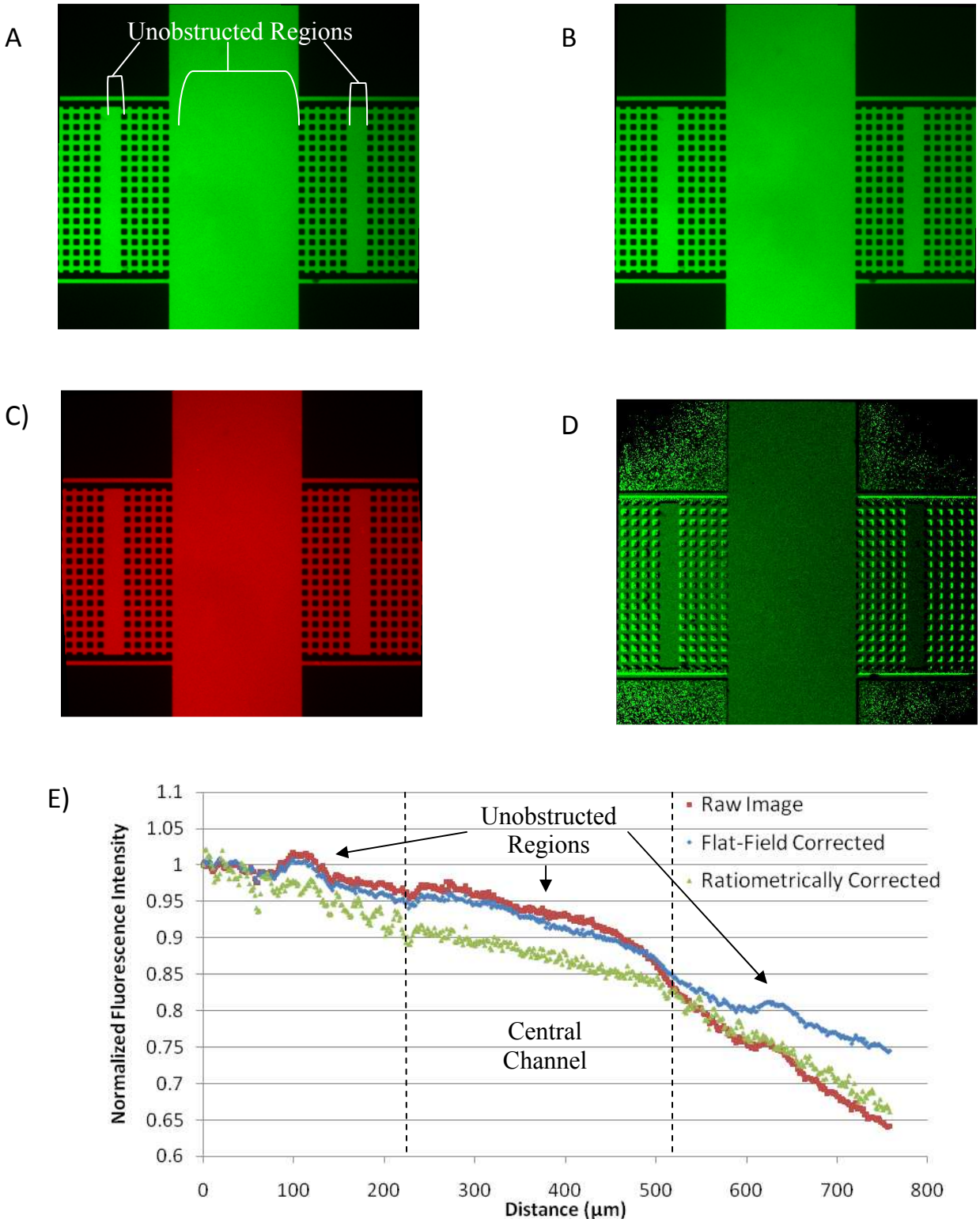

Figure 6 – Flat-field and ratiometric image correction of a field of view traversing the central channel. A) An uncorrected image of the gradient forming fluorophore with the three unobstructed regions labeled. B) Image corrected by standard flat-field methods described in Eq. (2). C) An uncorrected image of the reference fluorophore. D) Image corrected by the two-color ratiometric method described in Eq. (3). E) Normalized intensity profiles generated along the direction of the gradient. Higher apparent intensity in the unobstructed regions of images without a ratiometric correction indicates that there is a loss of fluorescence intensity in the proximity of microstructures.

by calculating the average pixel intensity along the length of the bridge, excluding the pixels that correspond to the posts. The non-ratiometrically corrected images in this set demonstrate a loss of fluorescence intensity in the proximity of the posts. This shadowing effect results in higher overall intensities in the three unobstructed regions of the field of view that are illustrated in **Figure 6A**. **Figure 6E** demonstrates that the flat-field correction, which uses a featureless correction image, does not affect the shadowing in the proximity of the microstructures. The use of the ratiometric correction, however, does lead to an intensity profile without higher apparent intensity regions in unobstructed regions.

Experimental Validation of Finite Element Model

In **Figure 7** we demonstrate the agreement of the earlier numerical model with the ratiometrically corrected intensity profile corresponding to **Figure 6D**. This indicates that the variation in intensity that we quantified for **Figures 6A and 6B** is an optical artifact, and that appropriate correction yields a concentration profile that conforms to our theoretical expectations. There does appear to be a difference in the structure of the signal in the region of the posts, indicating that we may not have been completely successful in eliminating the effects of microstructure on fluorescence intensity. This, in turn, indicates that the ratiometric process could benefit from further optimization.

Gradient Quantification along the Optical Axis

While we show that the ratiometric method is appropriate for correcting the 2-D plane in best focus, the process is insufficient for accurate correction of the concentration profile with depth in the example device. As mentioned earlier, the time to equilibration in the axial

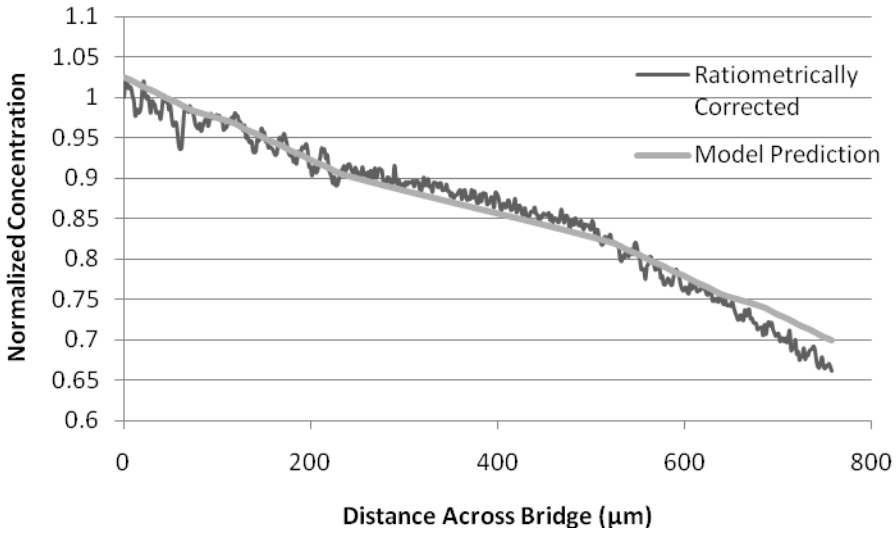

Figure 7 – The ratiometrically corrected data from Figure 6 and the corresponding model data are plotted as a function of distance along the bridge, normalized to the same maximum concentration.

dimension is much faster than equilibration of the gradient between reservoirs, so we expect a uniform axial concentration for this device's aspect ratio over the time frames of these trials. A first step to the correction process is determining whether the axial intensity profiles of the two fluorophores are similar enough that applying a ratiometric correction will correct the variation that results from translation in z. **Figure 8** demonstrates that there is some type of non-uniform height-dependent variation between the profiles of the two Alexa Fluors with distance into the channel. Calculating a simple ratio between the two does not yield the theoretically constant profile across the channel height.

Modeling of Cell Occlusion and Cell Spreading Effects on Gradient Development

With the use of micron size features in a microfluidic system, it becomes important to analyze how the introduction of cells alters the effective geometry of the device. The parameter of interest in a chemotaxis assay is the gradient that each cell encounters or, more precisely, the distribution of gradients that we expect our population of cells to be exposed to when conducting a trial. A researcher should consider both the average value and spread of this distribution, since these factors could relate to the average motility of cells and the observed heterogeneity in cell behavior. To demonstrate a numerical approach to calculating gradient sensitivity, we first modify the percent occlusion caused by loaded cells, which is a function of both aspect ratio and cell height. Based on images of actual cell loading, we generate a potential probability distribution of cell loading (**Figure 9A**). We simulate multiple trials in which cells are placed according to this probability distribution and aggregate the results for 200 cells of each occlusion condition. In **Figure 9B,** we quantify the gradients that cells encounter at time $\tau/2$, which corresponds to approximately 6 hours for the dextran-conjugated fluorophores utilized in this

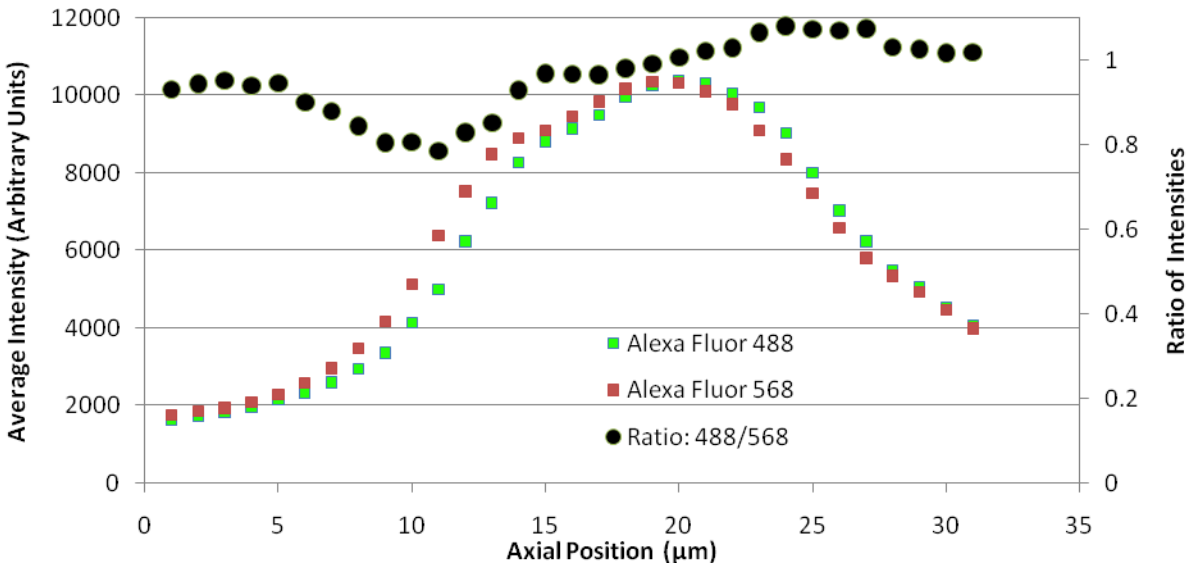

Figure 8 – Intensity profiles of both fluorophores across a 13 µm height channel. Scanning across a height of 35 µm in confocal mode demonstrates significant out-of-plane fluorescence. The non-uniform ratio of the two fluorophores outside the plane of best of focus indicates the inadequacy of this method for axial correction.

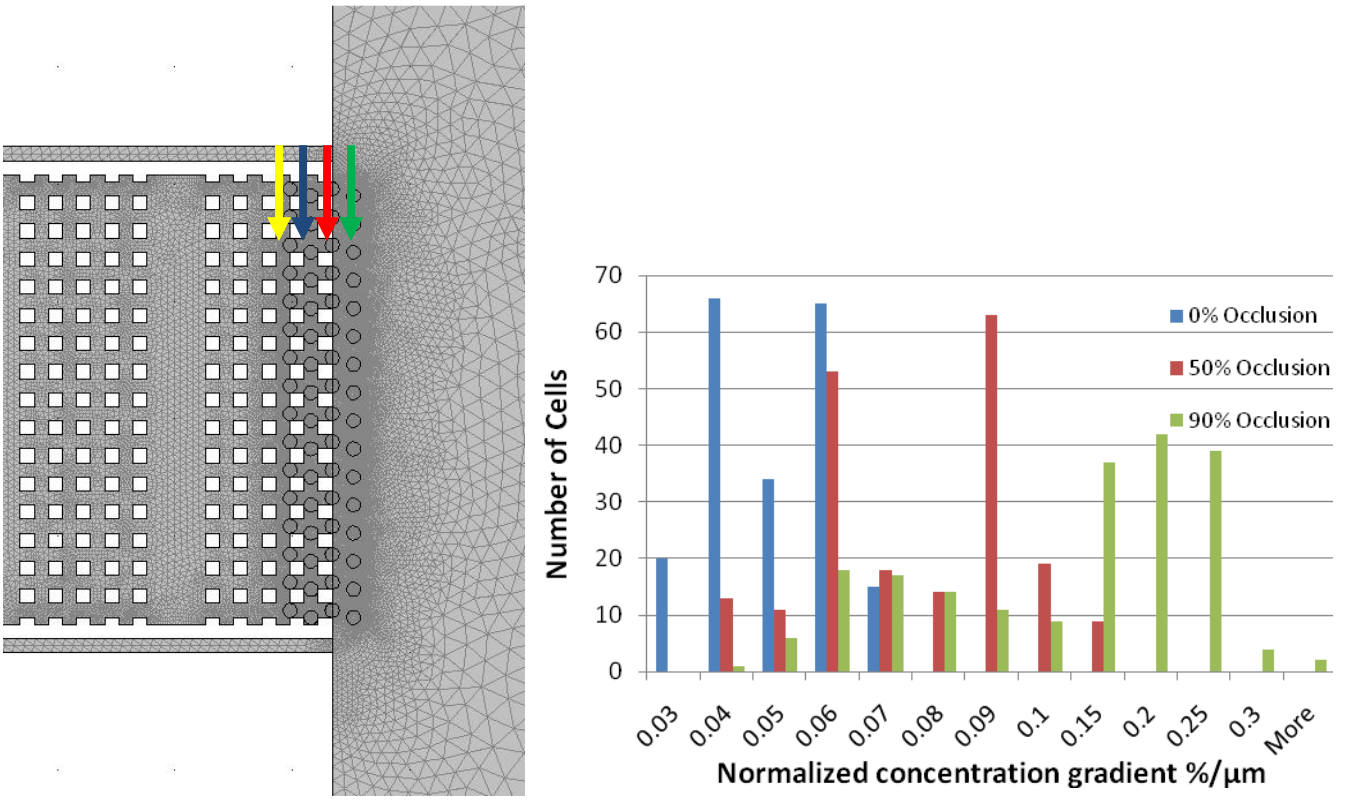

Figure 9 – Finite element model utilized to investigate the effects of cell geometry on the distribution of gradients experienced by the cells. A) At each position a cell, indicated by a small circle, was placed with a probability: Yellow – 20%.; Blue – 40%; Red – 70%; Green – 40%. B) 200 cells of each of three relative cell heights were analyzed to demonstrate the shift in average gradient and the dispersion of the gradient

experiment. These data demonstrate that both the average gradient that cells see becomes much steeper and that the distribution becomes much wider as the occlusion increases. In the idealized case of the cells not occluding the device (0%, Blue), they would be exposed to gradients ranging from .027%/μm to .068%/μm. If the cells occluded 50% of the height of channels they occupied (Red), the gradients would range from .037 %/μm to .116 %/μm, whereas the numbers would change to .033 %/μm to .310 %/μm for 90% occlusion (Blue). The mean and standard deviation shift accordingly, from a mean of .045 and standard deviation of .010 for the 0% occlusion condition, to a mean of .071 and standard deviation of .019 for 50% occlusion, and a mean of .139 with a standard deviation of .066 for the 90% occlusion condition. The steeper average gradient results from the lower effective diffusivity across highly occluded regions of the device, while the dispersion of gradients results from the distorting effect of cells on surrounding regions.

While it is possible that cells can distort gradients significantly, the modeling process suggests two factors that can potentially minimize the effect. By increasing the aspect ratio of the device, the percent occlusion will drop accordingly, shifting the gradient distribution towards the idealized zero cell thickness case. The biology of the cell motility process can also be helpful; since many cells spread across the substrate before becoming motile, they often occlude less volume than immediately after loading. To simulate this, we first considered a set of cells that have occluded the device at 50% of the channel height until time $\tau/2$. Since flattened cells can spread to a thickness of as little as 1-2 μm, we then allowed the cells to flatten and occlude only 10% of the channel height. In **Figure 10** we examine the gradients encountered by a population of 200 cells at the initial time point of spreading and over the course of a further $\tau/2$. The average gradient encountered by the cells decreases rapidly after allowing for cell spreading; the mean

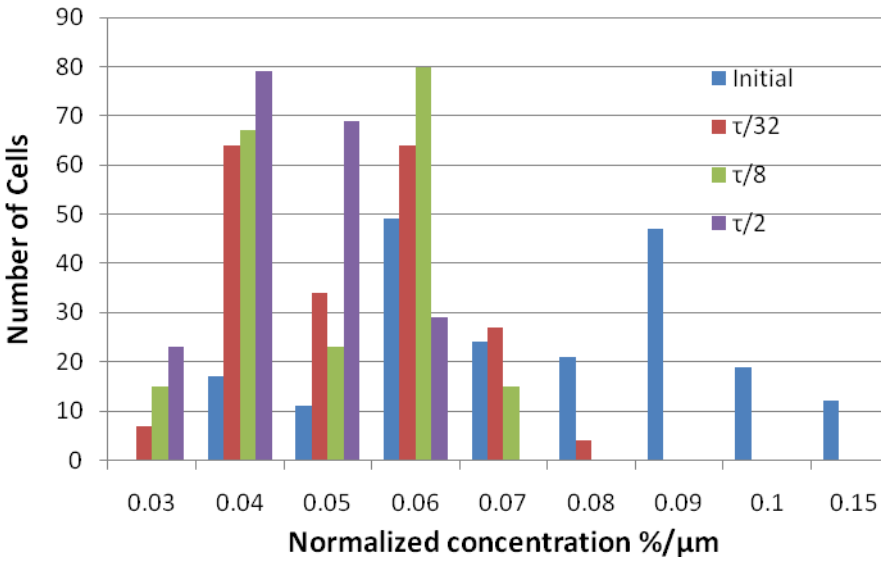

Figure 10 – Utilizing the finite element model from Fig. 9A, the effects of cell adhesion on the time evolution of the gradient were analyzed. After a period of $\tau/2$ elapsed with 50% occlusion, the cell occlusion is reduced to 10% to simulate the decrease in height associated with the cellular spreading process. This histogram corresponds to the distribution of gradients encountered by an aggregated 200 cell population for several time points after adhesion. The shift in the distribution of gradients over a period of less than τ demonstrates the rapid restitution of the increased gradient back to the design value.

falls from .070 to .048 within the first $\tau/32$, and then decreases more gradually to .0474 after $\tau/8$ and .040 after $\tau/2$. The variation of the gradients encountered by the cells follows a similar pattern, declining rapidly from .019 to .012 after $\tau/32$ and then slowly approaching .010 at $\tau/2$. The rapid adjustment of the gradient is a consequence of the relative scale of the cells. Since the gradient recovery process is a function of diffusion, which varies as $1/L^2$, equilibration along the length of the cell can occur more rapidly than gradient development across the entire bridge.

Modeling of Cell Loading Density on Gradient Formation

Much as the choice of aspect ratio can alter how extensively the cells affect the surrounding gradient, cell loading density can directly alter the gradients encountered by the cells. As a first order approximation, we assumed that the relative proportions of cells along the positions in **Figure 9A** are unchanged and that cells occlude 50% of the channel height, but we increased and reduced the expected number of cells by a factor of two. Where the probability would exceed 100%, we assumed that there will always be a cell present in that location. Once again aggregating the data for 200 cells of each condition, we demonstrate graphically the spread in gradients experienced by the populations of cells in **Figure 11**. There is little difference in the mean and dispersion of the gradients of the cells at standard and 50% loading densities. When increasing cell density to twice the standard value, however, the mean and dispersion of the gradients encountered by the cells increase by approximately 10% each. This seems to indicate that beyond a threshold in cell density, the dependence of gradient formation on further changes in cell density could confound data collected without careful control of cell numbers.

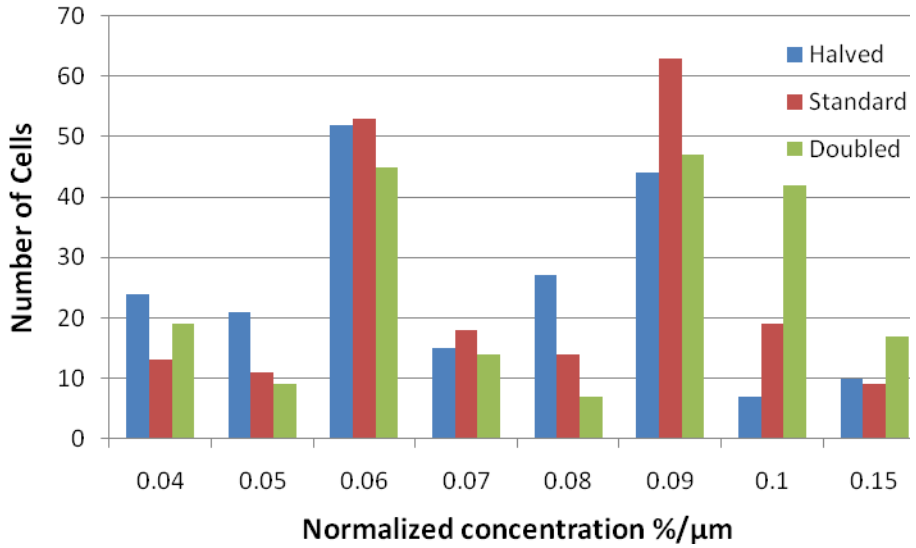

Figure 11 – Utilizing the finite element model from Fig. 9A, the effects of cell loading density on the distribution of gradients encountered by the cells were analyzed. Cell loading density was halved and doubled by adjusting the probabilities mentioned in Fig. 9 while maintaining a relative cell height of 50% occlusion.

Discussion

Representative Chemotaxis Device

While the theoretical underpinnings and biological significance of this device are discussed elsewhere, the motivations for the chosen system are presented briefly. The challenges of developing a precise, quantifiable chemotactic system have been taken on by a multitude of microfluidic researchers, resulting in many question-specific systems [40]. Despite the applicability and potential impact of these systems to biological research, many biologists lack access to a collaborating microfluidics laboratory and rely on older *in vitro* systems such as the Boyden chamber. While this system provides a porous substrate for migration, read-out is traditionally done by allowing cells to migrate for a pre-determined time and then counting the number of cells that are on either side of the membrane. Much required information cannot be obtained, for example, dynamic information on cell motility; instead, one simply counts the number of cells that cross the filter in a particular time interval, and it is not possible to determine if there are multiple cellular phenotypes present such as a mixed population of fast- and slow-migrating cells. Finally, the time frame of migration in the membrane may not be physiologically relevant and any dispersion in the sizes of the pores in the membrane could skew the results of the assay [41].

The PDMS system diagrammed in **Figure 1** has regular structures produced to a tight tolerance, is optically transparent and is amenable to high-throughput assessment of chemotaxis by established automated nuclei counting methods [42]. This system also allows for the continuous imaging and quantification of the cell actually undergoing the chemotaxis process in this pore-like environment. Four experiments can be conducted within a single device,

corresponding to the four "bridges" connecting the reservoirs. Minor changes to device geometry allow for each of these bridges to provide a different gradient. Since soft lithography minimizes any variation in post spacing, the confounding factor of pore size in the Boyden chamber is eliminated. This device also avoids the flow-based artifacts on cell motility that may be associated with pressures across macro-scale devices or that may be present in active gradient generators.

Simultaneous application in our device of a chemical stimulus by the gradient and mechanical stimuli by the posts will help elucidate effects of the physical environment on behaviors otherwise treated as purely chemotactic responses [43]. Post structures, or the equivalent in similar systems, can provide three-dimensional constraints that mimic cellular microenvironments, constrain cells of a certain size or stiffness, or serve as surfaces for functionalization with molecules that affect cell adhesion or cellular traction forces. The chemical and mechanical stimuli that are provided by the system may not be independent, however, and it becomes important to analyze their interdependence through modeling and empirical analysis. Cells self-sort in the system based on their ability to invade or migrate while responding to a combination of cues. This will prove to be a valuable assay and separation method since, for example, heterogeneity in cancerous cell populations is often reflected by differences in cellular motility [44, 45]. In summary, three-dimensional chemotaxis systems of this type will be important to exploring the integrated response of cells in a more life-like environment, but they also raise the need for a rigorous analysis of distortion in the gradient due to cells and device geometry.

Effects of Device Microstructure on Gradient Formation

When traversing a row of posts, the cross-sectional area in the *xy* plane of the microfluidic channels for gradient formation is at a minimum, and the gradient is nearly twice as steep. This has several consequences for our system. It is reasonable to treat the gradient as pseudo-stable in time because the spatial variation is significantly greater than the dependence of the gradient on the passage of time during the length of biologically relevant experiments. In conducting assays with this system, however, it will be important to note that the behavior of cells in the regions of the post cannot be attributed solely to mechanical cues since the gradient also varies. Since this component of the model is conducted in two dimensions by considering only the obstruction that the PDMS posts provide in the *xy* plane, the effect is independent of channel height. If this spatial variation was of concern to the experimenter, the *xy* footprint of the posts, the post spacing, or the height of the posts in *z* could be altered to reduce the spatial dependence of gradient steepness.

While this model, based on simple Fickian diffusion, demonstrates variation of the gradient of over a factor of two along the length of the bridge, an unwary experimenter looking only at concentration profiles in a microfluidic device may easily miss the effect. For example, if data taken from this model are analyzed under the assumption of a perfectly linear gradient, the absolute value of the resulting correlation coefficient would be >0.99. Without the use of complementary analytical and computational tools, incorrect expectations of gradient shape could easily lead to inaccurate conclusions.

Consequences of High Fluorophore Concentration and the Use of Multiple Fluorophores

Before attempting to use a multi-color correction method to address the problems described above, we must determine what effects the use of multiple fluorophores will have on

the quantification process. In the basic case of exciting a single fluorophore at low concentrations, an experimenter can expect an effectively linear relationship between fluorophore concentration and emission intensity [14]. This linear relationship, however, is based on several assumptions that must be re-analyzed in the context of the multi-dye two- and three-dimensional imaging methods presented here. When light of the exciting wavelength passes through a sample, it is being absorbed and dissipated throughout according to the Beer-Lambert Law. Because of this absorption, the amount of light available to excite fluorophores decreases throughout the thickness of the sample. As a result, a collection of fluorophores farther from the light source would emit correspondingly less total fluorescence. The height-dependent absorption would interfere with the linearity of the relationship between concentration and fluorescence intensity since the loss of light through the sample would be more significant at higher concentrations. High concentrations can also lead to quenching in which excited fluorophores will lose energy by thermal processes instead of by emitting a detectable photon [14]. Since absorption reduces the illumination as a function of height through the sample, attempts to measure gradients in three dimensions would be confounded. At low enough concentrations, however, a negligible amount of light is absorbed through the entire thickness of the sample. In this case, assuming a linear relationship between concentration and recorded intensity would be reasonable, and concentration profiles could be derived axially through any type of optical sectioning.

We also consider the effects of cross-talk between the fluorophores on linear response. Even with optimized filters for excitation, both fluorophores will absorb light at both of the excitation wavelengths since the excitation process follows a spectral absorption curve. Since we showed that even at its peak absorbance neither fluorophore will absorb more than 2% of the

illuminating light, we do not need to worry about attenuation of one fluorophore's excitation by the other. To determine whether either fluorophore is being significantly excited at the other's wavelength, we compared the corresponding absorption spectra (**Figure 4**). At an excitation wavelength of 488 nm, the Alexa Fluor 568 is only 3% as absorptive as the Alexa Fluor 488. At an excitation wavelength of 568 nm, the effect is a bit more pronounced with a cross absorption of 11%. The contribution to bleed-through, however, is even lower than these values since the emission filters are also chosen to be specific for the fluorophore of interest. This analysis does raise the point, however, that at very disparate concentrations bleed-through is possible, and the existence of a second fluorophore acts to raise the limit of detection of the first. In conclusion, attention should be paid to ensure that the use of multiple fluorophores does not introduce new aberrations that overcome the potential advantages of the ratiometric method.

Quantification of Fluorescence Intensity through Ratiometric Image Correction

In a relatively simple architecture like the two-layer device analyzed in this work, the concentration gradients could be analyzed piecewise to obtain meaningful quantitative data as long as the experimenter is willing to make assumptions about concentration continuity at height boundaries. In microfluidic systems with more complex geometries or sources at different heights, however, the dependence of intensity on channel height might preclude quantification. While fluorescence microscopy is often idealized to the interrogation of a single plane of the sample, the fact that microscope components will project cones of illumination and collection onto a single measured pixel becomes relevant in this multi-height situation. Fluorophore molecules above and below the plane of interest are illuminated, if not as efficiently as those on the focal plane. Similarly, light from any plane outside of the focal plane is minimal, but

summation across the height of the collection cone becomes significant enough to cause the variation noted in **Figure 5** when utilizing the single-color flat-field correction.

We suspect two related factors contributed to the shadowing effect noted in **Figure 6**. The value that is recorded for a single pixel on the CCD camera, as mentioned above, corresponds to an illumination and collection cone generated by the objective. Depending on the numerical aperture, shadowed regions will have portions of these cones obstructed by adjacent posts, reducing the total intensity collected. The refraction index mismatches at interfaces may also lead to light being improperly trapped and redirected in the PDMS in the same manner as an optical fiber directs light, an effect known as light-piping. While this effect is actually utilized in on-chip optical elements, to our knowledge, standard quantitative imaging methods are not available to correct for this loss [46].

Since the microtopography of the device has such a drastic effect on the illumination and read-out of a field of view, we evaluated the concept of a field-specific ratiometric correction in this work. Like existing ratiometric methods for quantifying intracellular calcium concentration [34], this process provides a numerical correction for differences in the path length and illumination throughout a three-dimensional sample. Unlike existing methods, however, we cannot rely on both a measurement and reference signal from a single fluorophore, so we introduce a uniformly distributed reference molecule. By no longer constraining ourselves to the subset of fluorophores that provide multiple read-out wavelengths, we can apply the ratiometric methodology in a more flexible way. Both the corrective capabilities indicated in **Figures 5E** and **6E** and the flexibility of the method indicate its potential for quantifying emission variation in topographies that confound traditional flat-field correction. It will also be worthwhile to determine whether there are chromatic aberrations associated with the PDMS-water interface.

Potential of Ratiometric Methods for the Study of Partitioning Effects

The ratiometric imaging process also allows us to explore the possibility of the partitioning of molecules into the surrounding PDMS. Many small hydrophobic molecules, such as organic pollutants, affect cell behavior but may be difficult to study in this format because of partitioning into PDMS structures [47]. While both molecules used in this experiment are too large and hydrophilic to partition into the surrounding polymer, this process could be repeated with a reference flurophore that cannot diffuse into the material and a second fluorophore with an unknown capacity to partition. A gradient of intensity within the corrected image of the posts would imply that the signal within the posts is actually a result of partitioning instead of a light-piping related artifact. The negative control case of two large fluorophore molecules would also have to be conducted, however, to distinguish the possibilities of light-piping, chromatic aberrations within the device, and small molecule partitioning.

Ratiometric Correction for the Measurement of Gradients along the Optical Axis

There may be several factors that lead to these non-uniform shifts in the *z* direction noted with respect to **Figure 8**. For example, incomplete correction of the chromatic aberration of the imaging system could contribute to the observed shift in *z*. While the imaging system may be color-corrected for the plane of best focus, it seems under- and over-corrected on either side. Any imperfection in the optics for the two laser colors would also contribute to the observed behavior. Finally, both the refractive index of the water and PDMS components of the sample show a dependence on light wavelength over the range we utilize [48, 49]. As a consequence, light of each wavelength will behave differently with increasing depth into the sample, confounding our attempts at quantitatively analyzing gradient formation along the optical *z* axis.

CHAPTER III

CONCLUSIONS AND FUTURE DIRECTIONS

Microfluidic devices have been making inroads as an experimental platform despite the difficulty of developing universal solutions and translating engineering advances into biological tools. Construction of a system on these scales has great potential for making chemotaxis assays more precise, reproducible, and amenable to analytic characterization. As researchers begin to investigate the integrated responses of cells by using the micron feature sizes of microfluidics to create a controlled microenvironment for cells, they will need new tools to eliminate confounding variables and accurately quantify experimental data.

In this work, we considered gradient formation in a microfluidic device with a complex topography and no replenishment of the chemoattractant. The effects of device geometry on local gradient formation were significant, and for this particular device we demonstrated that gradients in the regions of posts were twice as steep as those in unobstructed regions. As we attempted to empirically quantify this spatial dependence on gradient formation, we were confounded by the effects of varying channel heights and of PDMS structures on quantitative fluorescence measurements.

To correct for differences in light path and light-piping effects in the proximity of structures, we utilized a novel ratiometric correction employing a second uniform reference fluorophore. While the ratiometric concept is not new, it has traditionally been limited to a single dye method for specific applications such as intracellular calcium measurement. To generalize this system for quantification of concentration gradients within our microfluidic devices, we

introduced a second fluorophore. We examined the possibility of cross-talk between the fluorophores, determining that deviations from linearity should be negligible for the fluorophore concentrations utilized. The ratiometric process proved an effective, though not complete, solution for these two categories of fluorescence differences. We also demonstrated agreement of experimental data with the basic Fickian models we proposed. Through further optimization, we believe that this method could allow for more accurate quantification of fluorescence in the complex microstructures that are becoming common in microfluidic design. We considered this method for quantifying fluorescence in three dimensions in conjunction with confocal microscopy. In our experience, different fluorophores demonstrate different dependencies on height, precluding the use of a reference fluorophore as a way of correcting for differences in illumination across the height of the sample.

By supplementing the ratiometric technique with an algorithm that takes into account the differences between fluorophores, it may be possible to overcome the difficulty associated with measuring gradients in the *z* axis. The ratiometric correction method could, for example, be used in conjunction with two-photon microscopy to minimize the contribution of out-of-plane components [50]. In microfluidic devices with high enough fluorophore concentrations to introduce cross-talk between the fluorophores, a linear un-mixing system could also allow for distinguishing the otherwise convoluted signals [51]. There is still significant work to be done to address the potential causes mentioned above for the variation between the fluorophores as a function of height. For example, illumination could be done in a broadband manner to eliminate alignment issues between lasers. This would require an appropriate filter set or spectrometer for separation of the emission wavelengths. Similarly, samples could be chosen with minimal dispersion in the visible wavelengths to eliminate that as a cause of error.

In the last component of this work, we considered the effect that the cells themselves have on gradient formation. Neglecting active remodeling of the gradient through cellular metabolism or production, we primarily analyzed the effect of cells on device geometry. By probabilistically inserting cell-shaped occlusions into the original finite element model of the system, we were able to examine how aspect ratio and cell loading density affected local gradients in the device. There is no single gradient associated with a set of device parameters, however, so we present data in terms of distributions of gradients. We showed that the distribution will shift upward in mean value and become more disperse as the effective cell height, or occlusion, increases. Fortunately for the examination of motile cells, the adhesion and flattening of cells are followed by rapid reduction in gradient steepness. We also demonstrated that the mean gradient that an average cell encounters will be a direct function of cell loading density. These conclusions have consequences for explaining the heterogeneity of cell behavior in microfluidic chemotaxis assays.

The approach we take in this work will become increasingly relevant as more interdisciplinary teams utilize microfluidic devices as a platform for asking biological questions that require precise measurements. While many applications can safely dismiss so-called optical edge effects near interfaces of substrate and fluid, the increasing demand for mimicking the entire cellular microenvironment will necessitate the inclusion of mechanical cues. If micropatterned structures are used to present these cues, accurate imaging in the proximity of these structures may prove to be important. By considering complementary methods for modeling and quantifying gradient formation in these complex systems, we present a suite of tools for the rational design and evaluation of gradient formation in microfluidics with features that have cell-sized dimensions.

REFERENCES

[1] S. K. Sia, and G. M. Whitesides, "Microfluidic devices fabricated in Poly(dimethylsiloxane) for biological studies," Electrophoresis, 24(21), 3563-3576 (2003).

[2] T. M. Squires, and S. R. Quake, "Microfluidics: Fluid physics at the nanoliter scale," Reviews of Modern Physics, 77(3), 977-1026 (2005).

[3] D. J. Beebe, G. A. Mensing, and G. M. Walker, "Physics and applications of microfluidics in biology," Annual Review of Biomedical Engineering, 4, 261-286 (2002).

[4] G. M. Walker, H. C. Zeringue, and D. J. Beebe, "Microenvironment design considerations for cellular scale studies," Lab on a Chip, 4(2), 91-97 (2004).

[5] J. P. Wikswo, A. Prokop, F. Baudenbacher *et al.*, "Engineering challenges of BioNEMS: the integration of microfluidics, micro- and nanodevices, models and external control for systems biology," Iee Proceedings-Nanobiotechnology, 153(4), 81-101 (2006).

[6] N. L. Jeon, S. K. W. Dertinger, D. T. Chiu *et al.*, "Generation of solution and surface gradients using microfluidic systems," Langmuir, 16(22), 8311-8316 (2000).

[7] D. Irimia, D. A. Geba, and M. Toner, "Universal microfluidic gradient generator," Analytical Chemistry, 78(10), 3472-3477 (2006).

[8] S. Faley, K. Seale, J. Hughey *et al.*, "Microfluidic platform for real-time signaling analysis of multiple single T cells in parallel," Lab on a Chip, 8(10), 1700-1712 (2008).

[9] Y. Wang, T. Mukherjee, and Q. Lin, "Systematic modeling of microfluidic concentration gradient generators," Journal of Micromechanics and Microengineering, 16(10), 2128-2137 (2006).

[10] B. R. Gorman, and J. P. Wikswo, "Characterization of transport in microfluidic gradient generators," Microfluidics and Nanofluidics, 4(4), 273-285 (2008).

[11] A. Khademhosseini, R. Langer, J. Borenstein *et al.*, "Microscale technologies for tissue engineering and biology," Proceedings of the National Academy of Sciences of the United States of America, 103(8), 2480-2487 (2006).

[12] J. J. Norman, J. M. Collins, S. Sharma *et al.*, "Microstructures in 3D biological gels affect cell proliferation," Tissue Engineering Part A, 14(3), 379-390 (2008).

[13] U. Haessler, Y. Kalinin, M. A. Swartz *et al.*, "An agarose-based microfluidic platform with a gradient buffer for 3D chemotaxis studies," Biomedical Microdevices, 11(4), 827-

835 (2009).

[14] D. Murphy, [Fundamentals of Light Microscopy and Electronic Imaging] Wiley-Liss, New York(2001).

[15] C. Beta, T. Frohlich, H. U. Bodeker *et al.*, "Chemotaxis in microfluidic devices - a study of flow effects," Lab on a Chip, 8(7), 1087-1096 (2008).

[16] S. Li, N. F. Huang, and S. Hsu, "Mechanotransduction in endothelial cell migration," Journal of Cellular Biochemistry, 96(6), 1110-1126 (2005).

[17] M. Iiizumi, W. Liu, S. K. Pai *et al.*, "Drug development against metastasis-related genes and their pathways: A rationale for cancer therapy," Biochimica Et Biophysica Acta-Reviews on Cancer, 1786(2), 87-104 (2008).

[18] P. Devreotes, "Dictyostelium-discoideum - A model system for cell-cell interactions in development," Science, 245(4922), 1054-1058 (1989).

[19] P. Devreotes, and C. Janetopoulos, "Eukaryotic chemotaxis: Distinctions between directional sensing and polarization," Journal of Biological Chemistry, 278(23), 20445-20448 (2003).

[20] S. Boyden, "The chemotactic effect of mixtures of antibody and antigen on polymorphonuclear leucocytes," J. Exp. Med., 115(3), 453-466 (1962).

[21] S. H. Zigmond, and S. J. Sullivan, "Sensory adaptation of leukocytes to chemotactic peptides," Journal of Cell Biology, 82(2), 517-527 (1979).

[22] D. Zicha, G. A. Dunn, and A. F. Brown, "A new direct-viewing chemotaxis chamber," Journal of Cell Science, 99, 769-775 (1991).

[23] Y. X. Liu, J. Q. Sai, A. Richmond *et al.*, "Microfluidic switching system for analyzing chemotaxis responses of wortmannin-inhibited HL-60 cells," Biomedical Microdevices, 10(4), 499-507 (2008).

[24] K. Lee, C. Kim, B. Ahn *et al.*, "Generalized serial dilution module for monotonic and arbitrary microfluidic gradient generators," Lab on a Chip, 9(5), 709-717 (2009).

[25] G. M. Walker, J. Q. Sai, A. Richmond *et al.*, "Effects of flow and diffusion on chemotaxis studies in a microfabricated gradient generator," Lab on a Chip, 5(6), 611-618 (2005).

[26] H. K. Wu, B. Huang, and R. N. Zare, "Generation of complex, static solution gradients in microfluidic channels," Journal of the American Chemical Society, 128(13), 4194-4195 (2006).

[27] A. Shamloo, N. Ma, M. M. Poo *et al.*, "Endothelial cell polarization and chemotaxis in a microfluidic device," Lab on a Chip, 8(8), 1292-1299 (2008).

[28] Y. Du, J. Shim, M. Vidula *et al.*, "Rapid generation of spatially and temporally controllable long-range concentration gradients in a microfluidic device," Lab on a Chip, 9(6), 761-767 (2009).

[29] S. Li, J. L. Guan, and S. Chien, "Biochemistry and biomechanics of cell motility," Annual Review of Biomedical Engineering, 7, 105-150 (2005).

[30] R. G. Thakar, M. G. Chown, A. Patel *et al.*, "Contractility-dependent modulation of cell proliferation and adhesion by microscale topographical cues," Small, 4(9), 1416-1424 (2008).

[31] A. Brock, E. Chang, C. C. Ho *et al.*, "Geometric determinants of directional cell motility revealed using microcontact printing," Langmuir, 19(5), 1611-1617 (2003).

[32] B. Mosadegh, C. Huang, J. W. Park *et al.*, "Generation of stable complex gradients across two-dimensional surfaces and three-dimensional gels," Langmuir, 23(22), 10910-10912 (2007).

[33] G. M. Walker, and D. J. Beebe, "A passive pumping method for microfluidic devices," Lab on a Chip, 2(3), 131-134 (2002).

[34] A. Takahashi, P. Camacho, J. D. Lechleiter *et al.*, "Measurement of intracellular calcium," Physiological Reviews, 79(4), 1089-1125 (1999).

[35] M. S. Williams, K. J. Longmuir, and P. Yager, "A practical guide to the staggered herringbone mixer," Lab on a Chip, 8(7), 1121-1129 (2008).

[36] J. C. McDonald, D. C. Duffy, J. R. Anderson *et al.*, "Fabrication of microfluidic systems in poly(dimethylsiloxane)," Electrophoresis, 21(1), 27-40 (2000).

[37] A. F. Mills, [Basic Heat and Mass Transfer] Prentice Hall, Los Angeles(1999).

[38] Z. H. Liang, N. Chiem, G. Ocvirk *et al.*, "Microfabrication of a planar absorbance and fluorescence cell for integrated capillary electrophoresis devices," Analytical Chemistry, 68(6), 1040-1046 (1996).

[39] R. Sjoback, J. Nygren, and M. Kubista, "Absorption and fluorescence properties of fluorescein," Spectrochimica Acta Part a-Molecular and Biomolecular Spectroscopy, 51(6), L7-L21 (1995).

[40] T. M. Keenan, and A. Folch, "Biomolecular gradients in cell culture systems," Lab on a Chip, 8(1), 34-57 (2008).

[41] G. Cinamon, and R. Alon, "A real time in vitro assay for studying leukocyte transendothelial migration under physiological flow conditions," Journal of Immunological Methods, 273(1-2), 53-62 (2003).

[42] H. Ancin, B. Roysam, T. E. Dufresne *et al.*, "Advances in automated 3-D image analysis of cell populations imaged by confocal microscopy," Cytometry, 25(3), 221-234 (1996).

[43] A. K. McNulty, M. Schmidt, T. Feeley *et al.*, "Effects of negative pressure wound therapy on fibroblast viability, chemotactic signaling, and proliferation in a provisional wound (fibrin) matrix," Wound Repair and Regeneration, 15(6), 838-846 (2007).

[44] M. Harris, E. Kim, B. Weidow *et al.*, "Migration of isogenic cell lines quantified by dynamic multivariate analysis of single-cell motility.," Cell Adh Migr, 2(2), 127-36 (2008).

[45] E. LaTulippe, J. Satagopan, A. Smith *et al.*, "Comprehensive gene expression analysis of prostate cancer reveals distinct transcriptional programs associated with metastatic disease," Cancer Research, 62(15), 4499-4506 (2002).

[46] D. A. Chang-Yen, R. K. Eich, and B. K. Gale, "A monolithic PDMS waveguide system fabricated using soft-lithography techniques," Journal of Lightwave Technology, 23(6), 2088-2093 (2005).

[47] J. H. Kwon, T. Wuethrich, P. Mayer *et al.*, "Dynamic permeation method to determine partition coefficients of highly hydrophobic chemicals between poly(dimethylsiloxane) and water," Analytical Chemistry, 79(17), 6816-6822 (2007).

[48] A. N. Bashkatov, and E. A. Genina, "Water refractive index in dependence on temperature and wavelength: a simple approximation," Proceedings of the SPIE - The International Society for Optical Engineering, 5068(1), 393-5 (2003).

[49] F. Schneider, J. Draheirn, R. Kamberger *et al.*, "Process and material properties of polydimethylsiloxane (PDMS) for Optical MEMS," Sensors and Actuators a-Physical, 151(2), 95-99 (2009).

[50] C. Xu, W. Zipfel, J. B. Shear *et al.*, "Multiphoton fluorescence excitation: New spectral windows for biological nonlinear microscopy," Proceedings of the National Academy of Sciences of the United States of America, 93(20), 10763-10768 (1996).

[51] T. Zimmermann, J. Rietdorf, A. Girod *et al.*, "Spectral imaging and linear un-mixing enables improved FRET efficiency with a novel GFP2-YFP FRET pair," Febs Letters, 531(2), 245-249 (2002).